

Potential role of a hybrid intraoperative probe based on OCT and positron detection for ovarian cancer detection and characterization

Yi Yang,¹ Nrusingh C. Biswal,¹ Tianheng Wang,¹ Patrick D. Kumavor,¹
Mozafareddin Karimeddini,² John Vento,² Melinda Sanders,³ Molly Brewer,^{1,4}
and Quing Zhu^{1,*}

¹University of Connecticut, Dept. of Electrical and Computer Engineering, Storrs, CT 06269, USA

²University of Connecticut Health Center, Division of Radiology, Farmington, CT 06030, USA

³University of Connecticut Health Center, Division of Pathology, Farmington, CT 06030, USA

⁴University of Connecticut Health Center, Division of Gynecologic Oncology, Farmington, CT 06030, USA

*zhu@engr.uconn.edu

Abstract: Ovarian cancer has the lowest survival rate of the gynecologic cancers because it is predominantly diagnosed in the late stages due to the lack of reliable symptoms and efficacious screening techniques. A novel hybrid intraoperative probe has been developed and evaluated for its potential role in detecting and characterizing ovarian tissue. The hybrid intraoperative dual-modality device consists of multiple scintillating fibers and an optical coherence tomography imaging probe for simultaneously mapping the local activities of ¹⁸F-FDG uptake and imaging of local morphological changes of the ovary. Ten patients were recruited to the study and a total of 18 normal, abnormal and malignant ovaries were evaluated *ex vivo* using this device. Positron count rates of 7.5/8.8-fold higher were found between malignant and abnormal/normal ovaries. OCT imaging of malignant and abnormal ovaries revealed many detailed morphologic features that could be potentially valuable for evaluating local regions with high metabolic activities and detecting early malignant changes in the ovary. These initial results have demonstrated that our novel hybrid imager has great potential for ovarian cancer detection and characterization during minimally invasive endoscopic procedures.

© 2011 Optical Society of America

OCIS codes: (170.4500) Optical Coherence Tomography; (170.3880) Medical and biological imaging; (170.3890) Medical optics instrumentation; (170.4440) ObGyn.

References and links

1. T. R. Rebbeck, H. T. Lynch, S. L. Neuhausen, S. A. Narod, L. Van't Veer, J. E. Garber, G. Evans, C. Isaacs, M. B. Daly, E. Matloff, O. I. Olopade, and B. L. Weber; Prevention and Observation of Surgical End Points Study Group, "Prophylactic oophorectomy in carriers of BRCA1 or BRCA2 mutations," *N. Engl. J. Med.* **346**(21), 1616–1622 (2002).
2. N. D. Kauff, J. M. Satagopan, M. E. Robson, L. Scheuer, M. Hensley, C. A. Hudis, N. A. Ellis, J. Boyd, P. I. Borgen, R. R. Barakat, L. Norton, M. Castiel, K. Nafa, and K. Offit, "Risk-reducing salpingo-oophorectomy in women with a BRCA1 or BRCA2 mutation," *N. Engl. J. Med.* **346**(21), 1609–1615 (2002).
3. W. A. Rocca, B. R. Grossardt, M. de Andrade, G. D. Malkasian, and L. J. Melton, "Survival patterns after oophorectomy in premenopausal women: a population-based cohort study," *Lancet Oncol.* **7**(10), 821–828 (2006).
4. J. S. Berek, E. Chalas, M. Edelson, D. H. Moore, W. M. Burke, W. A. Cliby, and A. Berchuck; Society of Gynecologic Oncologists Clinical Practice Committee, "Prophylactic and risk-reducing bilateral salpingo-oophorectomy: recommendations based on risk of ovarian cancer," *Obstet. Gynecol.* **116**(3), 733–743 (2010).
5. N. Pandit-Taskar, "Oncologic imaging in gynecologic malignancies," *J. Nucl. Med.* **46**(11), 1842–1850 (2005).
6. M. Piert, M. Burian, G. Meisetschlager, H. J. Stein, S. Ziegler, J. Nahrig, M. Picchio, A. Buck, J. R. Siewert, and M. Schwaiger, "Positron detection for the intraoperative localisation of cancer deposits," *Eur. J. Nucl. Med. Mol. Imaging* **34**(10), 1534–1544 (2007).
7. F. Bogalhas, Y. Charon, M.-A. Duval, F. Lefebvre, S. Palfi, L. Pinot, R. Siebert, and L. Ménard, "Development of a positron probe for localization and excision of brain tumours during surgery," *Phys. Med. Biol.* **54**(14), 4439–4453 (2009).

8. H. W. Strauss, C. Mari, B. E. Patt, and V. Ghazarossian, "Intravascular radiation detectors for the detection of vulnerable atheroma," *J. Am. Coll. Cardiol.* **47**(8 Suppl), C97–C100 (2006).
9. B. E. Patt, J. S. Iwanczyk, L. R. MacDonald, Y. Yamaguchi, C. R. Tull, M. Janecek, E. J. Hoffman, W. Strauss, R. Tsugita, and V. Ghazarossian, "Intravascular probe for detection of vulnerable plaque," *Proc. SPIE* **4508**, 88–98 (2001).
10. V. E. Strong, J. Humm, P. Russo, A. Jungbluth, W. D. Wong, F. Daghighian, L. Old, Y. Fong, and S. M. Larson, "A novel method to localize antibody-targeted cancer deposits intraoperatively using handheld PET beta and gamma probes," *Surg. Endosc.* **22**(2), 386–391 (2008).
11. S. Yamamoto, K. Matsumoto, S. Sakamoto, K. Tarutani, K. Minato, and M. Senda, "An intra-operative positron probe with background rejection capability for FDG-guided surgery," *Ann. Nucl. Med.* **19**(1), 23–28 (2005).
12. R. R. Raylman, "Performance of a dual, solid-state intraoperative probe system with ^{18}F , $^{99\text{m}}\text{Tc}$, and (^{111}In) ," *J. Nucl. Med.* **42**(2), 352–360 (2001).
13. N. Auricchio, G. D. Domenico, L. Milano, R. Malaguti, G. Ambrosi, M. Ionica, E. Fiandrini, and G. Zavattini, "Characterization of silicon detectors for the SiliPET Project: a small animal PET scanner based on stacks of silicon detectors," *IEEE Trans. Nucl. Sci.* **57**(5), 2424–2436 (2010).
14. M. P. Tornai, B. E. Patt, J. S. Iwanczyk, C. R. Tull, L. R. MacDonald, and E. J. Hoffman, "A novel silicon array designed for intraoperative charged particle imaging," *Med. Phys.* **29**(11), 2529–2540 (2002).
15. D. Huang, E. A. Swanson, C. P. Lin, J. S. Schuman, W. G. Stinson, W. Chang, M. R. Hee, T. Flotte, K. Gregory, C. A. Puliafito, and J. G. Fujimoto, "Optical coherence tomography," *Science* **254**(5035), 1178–1181 (1991).
16. V. J. Srinivasan, Y. Chen, J. S. Duker, and J. G. Fujimoto, "*In vivo* functional imaging of intrinsic scattering changes in the human retina with high-speed ultrahigh resolution OCT," *Opt. Express* **17**(5), 3861–3877 (2009).
17. R. K. Wang, L. An, P. Francis, and D. J. Wilson, "Depth-resolved imaging of capillary networks in retina and choroid using ultrahigh sensitive optical microangiography," *Opt. Lett.* **35**(9), 1467–1469 (2010).
18. L. Yu and Z. Chen, "Doppler variance imaging for three-dimensional retina and choroid angiography," *J. Biomed. Opt.* **15**(1), 016029 (2010).
19. G. J. Tearney, H. Yabushita, S. L. Houser, H. T. Aretz, I. K. Jang, K. H. Schlendorf, C. R. Kauffman, M. Shishkov, E. F. Halpern, and B. E. Bouma, "Quantification of macrophage content in atherosclerotic plaques by optical coherence tomography," *Circulation* **107**(1), 113–119 (2003).
20. P. Barlis, P. W. Serruys, N. Gonzalo, W. J. van der Giessen, P. J. de Jaegere, and E. Regar, "Assessment of culprit and remote coronary narrowings using optical coherence tomography with long-term outcomes," *Am. J. Cardiol.* **102**(4), 391–395 (2008).
21. P. A. Testoni and B. Mangiavillano, "Optical coherence tomography in detection of dysplasia and cancer of the gastrointestinal tract and bilio-pancreatic ductal system," *World J. Gastroenterol.* **14**(42), 6444–6452 (2008).
22. M. J. Cobb, J. H. Hwang, M. P. Upton, Y. C. Chen, B. K. Oelschlagel, D. E. Wood, M. B. Kimmy, and X. Li, "Imaging of subsquamous Barrett's epithelium with ultrahigh-resolution optical coherence tomography: a histologic correlation study," *Gastrointest. Endosc.* **71**(2), 223–230 (2010).
23. J. B. McNally, N. D. Kirkpatrick, L. P. Hariri, A. R. Tumlinson, D. G. Besselsen, E. W. Gerner, U. Utzinger, and J. K. Barton, "Task-based imaging of colon cancer in the Apc(Min/+) mouse model," *Appl. Opt.* **45**(13), 3049–3062 (2006).
24. E. M. Kanter, R. M. Walker, S. L. Marion, M. Brewer, P. B. Hoyer, and J. K. Barton, "Dual modality imaging of a novel rat model of ovarian carcinogenesis," *J. Biomed. Opt.* **11**(4), 041123 (2006).
25. L. P. Hariri, G. T. Bonnema, K. Schmidt, A. M. Winkler, V. Korde, K. D. Hatch, J. R. Davis, M. A. Brewer, and J. K. Barton, "Laparoscopic optical coherence tomography imaging of human ovarian cancer," *Gynecol. Oncol.* **114**(2), 188–194 (2009).
26. C. L. Evans, I. Rizvi, T. Hasan, and J. F. de Boer, "*In vitro* ovarian tumor growth and treatment response dynamics visualized with time-lapse OCT imaging," *Opt. Express* **17**(11), 8892–8906 (2009).
27. M. A. Brewer, U. Utzinger, J. K. Barton, J. B. Hoying, N. D. Kirkpatrick, W. R. Brands, J. R. Davis, K. Hunt, S. J. Stevens, and A. F. Gmitro, "Imaging of the ovary," *Technol. Cancer Res. Treat.* **3**(6), 617–627 (2004).
28. J. Gamelin, Y. Yang, N. Biswal, Y. Chen, S. Yan, X. Zhang, M. Karemeddini, M. Brewer, and Q. Zhu, "A prototype hybrid intraoperative probe for ovarian cancer detection," *Opt. Express* **17**(9), 7245–7258 (2009).
29. D. Piao, M. M. Sadeghi, J. Zhang, Y. Chen, A. J. Sinusas, and Q. Zhu, "Hybrid positron detection and optical coherence tomography system: design, calibration, and experimental validation with rabbit atherosclerotic models," *J. Biomed. Opt.* **10**(4), 044010 (2005).
30. S. Cherry, J. Sorenson, and M. Phelps, *Physics in Nuclear Medicine*, 3rd. ed. (Saunders, 2003).
31. B. Meller, K. Sommer, J. Gerl, K. von Hof, A. Surowiec, E. Richter, B. Wollenberg, and M. Baehre, "High energy probe for detecting lymph node metastases with ^{18}F -FDG in patients with head and neck cancer," *Nucl. Med. (Stuttg.)* **45**(4), 153–159 (2006).
32. B. L. Franc, C. Mari, D. Johnson, and S. P. Leong, "The role of a positron- and high-energy gamma photon probe in intraoperative localization of recurrent melanoma," *Clin. Nucl. Med.* **30**(12), 787–791 (2005).

1. Introduction

Ovarian cancer has the lowest survival rate of the gynecologic cancers because it is predominantly diagnosed in Stages III and IV due to the lack of reliable symptoms as well as the lack of efficacious screening techniques. High risk women, who warrant screening because of their increased prevalence of the disease, do not have an effective screening tool to detect early cancers. In 2002, two landmark studies [1,2] were published on the benefit of

prophylactic oophorectomy (PO) which has become accepted as the standard of care for women carrying a BRCA 1 or 2 mutations. PO reduces the risk of ovarian cancer by more than 80%. In the absence of reliable methods of early detection of ovarian cancer, PO has been proposed as the most effective way to prevent this potentially lethal disease in this group of women. Although PO is effective in preventing breast and ovarian cancer, it has been recently found to increase mortality of women undergoing oophorectomy prior to the age of 45 [3] or even before the age of 55-60 [4]. These high risk women are not candidates for hormone replacement therapy because of their increased risk of breast cancer [3]. Thus, there is an urgent need to minimize the use of PO which is the major rationale for developing better and more sensitive tools to effectively evaluate the ovary during minimally invasive surgery.

Positron emission tomography (PET), using ^{18}F -fluoro-2-deoxy-d-glucose (^{18}F -FDG) as a tracer, can detect malignant cancers with altered glucose metabolism. However, it has limited value in lesion localization in early stages of ovarian cancer because of the difficulty in distinguishing between the signal from early-stage cancers and the background uptake signals coming from the normal tissue [5]. The average tissue path length of 511 keV gamma ray produced by ^{18}F -FDG is about 10 centimeters. As a result, the gamma signal from a small tumor is contaminated by the signal from the surrounding healthy tissue. Intraoperative probes which are selectively sensitive to short-range beta radiation have the significant advantage of detecting early-stage cancers [6,7]. The average tissue path length for ^{18}F beta particles (β 633.5keV) is a few millimeters [8] and it corresponds well with targeted internal organs, such as ovary, colon, and cardiac vessels before these particles interact with electrons to produce annihilating 511 keV gamma photons. A number of investigators are developing intraoperative or intravascular radiation detection systems for the early detection of cancers or atherosclerosis [6–10]. Many of the detectors proposed for use in beta-sensitive probes have utilized plastic scintillators [7–9,11], which convert ionizing particles into photons. In addition to scintillation detectors, solid-state devices have also been proposed for use in beta probes [12]. Furthermore, several groups have designed and built imaging beta cameras [13,14]. While these groups are developing radiation detectors for intraoperative or intravascular use, we have linked this type of functional intraoperative radiation detection with Optical Coherence Tomography (OCT) device that allows simultaneous high-resolution imaging of tissue morphology. OCT is an emerging high resolution imaging technique which measures backscattered light generated from an infrared light source directed at the tissues being examined [15]. OCT typically obtains a resolution capability of 5–15 μm and a depth of penetration of 1-2 mm and has been used to image tissues in the body that can be accessed either directly or via endoscope or catheter, including the eye [16–18], coronary blood vessels [19,20], GI track [21,22], colon [23] and ovary [24–27]. OCT is sensitive to collagen changes which were seen as malignancy develops [27].

In our previous publication [28,29], we introduced a novel hybrid intraoperative imaging device, which integrates multiple scintillating fibers and an OCT imaging probe for mapping the local uptake of ^{18}F -FDG and imaging morphological details of the rabbit atherosclerotic model and ovary. This hybrid imager has potential applications in ovarian cancer screening and diagnosis during minimally invasive endoscope procedures. In this paper, we report the first *ex vivo* studies of 18 normal, abnormal and malignant ovaries obtained from 10 human patients using this device.

2. Methods

2.1. Hybrid probe

The hybrid probe, which is shown within the blue dashed rectangle in Figs. 1(a-b), consists of a side-view ball lens OCT fiber and ten plastic scintillating fibers. The side and tissue surface views of the hybrid probe are shown in Figs. 1(c-d), and the photographs of the probe and the experimental setup are shown in Figs. 1(e-f). The central OCT fiber of diameter 0.5mm scans the 3-D volume of 2 mm (depth) \times 5 mm (lateral) \times 7 mm (longitudinal) underneath the probe. The ten scintillating fibers straddle the OCT channel in the arrangement of 2 \times 4 for

positron detection and 1×2 for gamma detection. The lateral spacing between two rows of scintillating fiber tips is 4.25 mm and the longitudinal spacing is 1.75 mm. Each scintillating fiber is a 3 mm long and 1 mm diameter plastic scintillating fiber (Saint-Gobain) epoxied to a plastic optical fiber of the same diameter and 1.2 meter long. The scintillating fiber tip is coated with reflective paint to enhance the light collection. The scintillating fibers are not only sensitive to positrons but also to gamma rays generated from positron annihilation in surrounding tissue. The high gamma background can therefore produce high background levels even with a positron-to-gamma sensitivity ratio of 10-13:1 typical of low-Z plastic scintillators [9,29]. In order to reduce the impact of gamma contamination, two separate 0.25 mm-thick Cu-shielded fibers measure the approximate gamma background levels that are then subtracted from the total detector counts. They are referred to as “beta-insensitive or gamma detectors”. The remaining eight scintillating detectors are referred to as “beta-sensitive or positron detectors”.

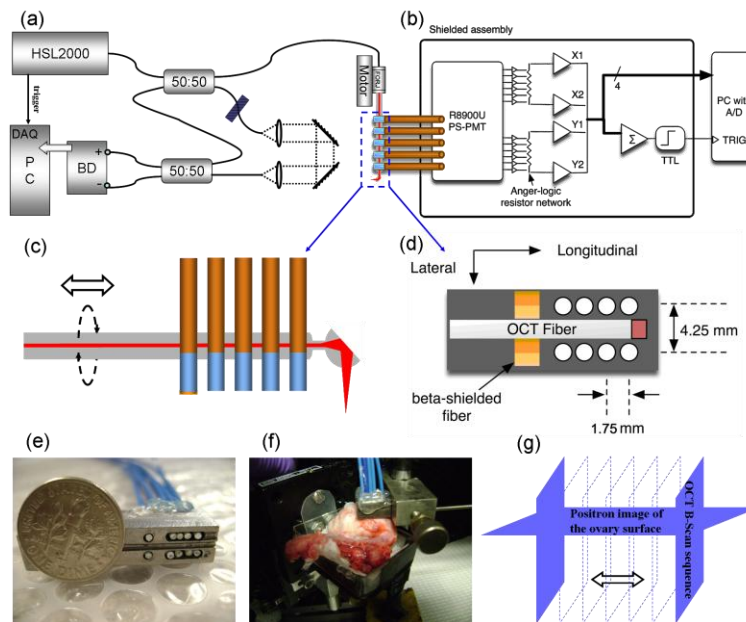


Fig. 1. (a) Schematic of swept-source OCT system. (b) Schematic of positron detection system. (c) Side view of the hybrid probe integrating OCT fiber and nuclear detectors. (d) Tissue surface view of the hybrid probe; (e) Photograph of the hybrid probe. (f) Experimental setup; (g) Co-registration scheme of surface positron distribution map and a sequence of OCT images.

2.2. OCT system

Figure 1(a) depicts the schematic of Fourier Domain OCT system which is based on a 110 nm bandwidth swept source (HSL-2000, Santec Corp., Japan) with center wavelength of 1310 nm and scan rate of 20 kHz. The 10 mW output power from the swept source was evenly split into reference and sample arms by a 2×2 coupler. A fiber optic rotary joint (Princeton Inc.) was inserted in the sample arm, to enable continuous circumferential scanning. The backscattered or back-reflected light was collected by a side view ball lens catheter (WT&T Inc., Canada) and recombined with the reference light at the second 2×2 coupler. The interferogram formed was detected by a balanced detector (Thorlabs PDB120C) and acquired by a 50 MHz digitizer (Cs8325, Gage Applied) after a 20 MHz anti-alias filter. The system sensitivity was 109dB and the axial resolution was approximately 12 μm in air. The lateral resolution of 25 μm was achieved at working distance of 1 mm away from the side surface of the catheter. For the reduced rotation rate of 16 seconds per revolution used in the initial demonstration, the A-scan rate was decreased to 250 Hz using a divider circuit. Therefore,

2000 A-lines were acquired for each frame corresponding to 180 degrees. Data processing and displaying were done at the time when the motor completed the rotation from 180 to 360 degrees. During image processing, a wavelength-dependent amplitude correction to the raw data was applied to account for the optical power variation during A-line scans. The scaled measurement data was interpolated to a uniform grid in k-space before Fourier transformation.

2.3. Positron Detection System

Figure 1 (b) depicts the configuration of the positron detection system composed of a position sensitive PMT (PSPMT, Hamamatsu R8900U), front-end electronics, and sampling-based multi-channel analyzer circuitry. The PSPMT provides 6 X and 6 Y readout anodes for position determination, which are in turn amplified and connected to a resistor divider network to provide four outputs: X1, X2 and Y1, Y2. Standard Anger logic is used to calculate the event position and the total event energy [30]. The PSPMT that is used has 64 light-sensitive detection areas, with each area measuring $2.5 \text{ mm} \times 2.5 \text{ mm}$. The ten scintillating input fibers separated by 2.5 mm were fed to the central region of the PSPMT, and the scattered photons that reached the areas outside of the central region were removed in the data processing. The positron counts from eight positron detectors were obtained by subtracting the average gamma background from the two beta-insensitive detectors. This was displayed as a positron distribution map or flood image and the summation was reported as the total counts. As each $2.5 \times 2.5 \text{ mm}^2$ detection area on the PSPMT was larger than the 1 mm diameter positron detector, the photons were proportionally distributed inside each circle of 1 mm diameter in the map. To determine the optimum counting time for the prototype probe and the system, the signal-to-background (SBR) ratio and the standard deviation ($n = 5$) vs. counting time using a 12.4 kBq ^{204}Tl source was evaluated. The background counts were obtained in the absence of the TI source. Within a 1-minute period, the SBR reached a peak and stayed there afterwards, while the standard deviation reduced to 3% of the mean value after 3 minutes and remained the same afterwards. Therefore, the positron counts were recorded for 3 minutes for all patients in the reported study.

The sensitivity of positron detectors was evaluated using ^{18}F -FDG radiotracer. This was done by filling a cylindrical glass well having a diameter of 25 mm with 0.5 ml ^{18}F -FDG of 3.84 MBq/ml, and then suspending the probe 0.5 mm above the ^{18}F -FDG level. The measured probe sensitivity was 9086 cps/MBq.

2.4. Patients

The clinical study was performed at the University of Connecticut Health Center (UCHC) from September 2009 to September 2010. The study protocol was approved by the Institutional Review Boards of UCHC and was HIPAA compliant. Signed informed consent was obtained from all patients. The eligible patients who were scheduled for oophorectomy were either at risk for ovarian cancer or they had an ovarian mass or pelvic mass suggesting malignancy. The study group consisted of ten patients whose ages ranged from 32 to 79 (mean 56). Two patients were premenopausal women and the rest were postmenopausal women. The ^{18}F -FDG was calibrated at the time of the injection with dose ranging from 484.7 MBq to 643.8 MBq (mean 557.4 MBq). Approximately, 35-45 minutes after the injection, the patient was transported to the operating room and prepared for surgery. Immediately after disruption of the blood supply, the ovaries were removed and transported to an adjacent lab for positron detection and OCT imaging. The time difference between injection and the first measurement for the ten patients varied from 77 to 145 minutes (mean 102 minutes). Typically, we started from the area pointed by the surgeon and then moved to other non-overlapping locations parallel to the long axis of the probe. This way, the histological samples could be cut consistently for correlating H&E stains with the OCT images. The positron distribution map corresponded to the probe plane and the sequence of OCT imaging planes was perpendicular to the probe plane as shown in Fig. 1(g). Depending on the size of the examined ovary, 3~9 non-overlapping areas were measured. All positron counts measured at different locations of the ovaries from the same patient were corrected to compensate for

radiation decay from that patient's injection time to the actual measurement time. Therefore, all the positron count rates of the different patients were compared at injection time and normalized to the injection dose. After positron detection and imaging, the ovaries were fixed in formalin and returned to the Pathology Department for histological processing. For histological evaluation, the ovaries were cut in 5 mm blocks parallel to the OCT imaging plane, dehydrated with graded alcohol, embedded in paraffin and sectioned to 7- μ m thickness using a paraffin microtome. Once the slides that correspond to the imaged planes were identified, they were stained using hematoxylin and eosin (H&E). In this study, two patients each had only one ovary available for this study. A total of eighteen ovaries from ten patients were investigated by our combined OCT and positron detection dual-modality system.

3. Results

3.1. Calibration

A simple quick calibration was applied right before each patient study by using 160 kBq ^{137}Cs (β 511.6 keV, γ 661.6 keV) sealed spherical source which was considered as a stable radionuclide with half-life 30.1 years. The radioactive source was placed 2mm under the center of the probe and monitored for 1 minute. The average total counts from eight positron detectors was 12035 ($n = 10$) and the standard deviation was 346 which was larger than the theoretically predicted value of 110 based on Poisson distribution. However, this small difference (2% of the total counts) can be explained by the slight different measurement conditions over this one year study period and the small sample size. The average of the total counts from two gamma detectors was 188 ($n = 10$) and the standard deviation was 30. We measured the beta-to-gamma sensitivity ratio of the scintillating fiber by placing a single fiber 2 mm above the 160 kBq ^{137}Cs source. The total gamma counts were measured by inserting a 0.25mm-thick Cu plate between the scintillating fiber and the source to shield the beta particles. A ratio of 11.4 was obtained as $(\text{total counts (beta + gamma)} - \text{gamma counts}) / (\text{gamma counts})$, with both measurements being five minutes long. This ratio agrees with the data from literature and our previous measurements [9,29]. Based on this ratio, we expect to get 243 counts for 2 beta-shielded scintillators as compared with the total 12035 counts obtained for the 8 beta sensitive scintillators. This small difference between predicted and measured can be explained by the slight different measurement conditions over this one year study period. Based on this calibration result, our nuclear detection sensitivity was about the same during this one-year patient study period.

3.2. Patient results

For the total of 10 patients studied, two patients had ovarian papillary serous carcinoma on both ovaries (#7 and #8), four patients had endometrial carcinoma (#3, #4, #6, #9), one patient had a benign dermoid tumor on one ovary (#10), one patient had enlarged ovaries of both sides (#1), and two patients had bilateral normal ovaries (#2, #5). To evaluate the metabolic activities of the ovaries from patients with endometrial cancer and compare their results with those obtained from patients with ovarian cancer, we have categorized this group of patients as the abnormal group. In addition, the right ovary of the patient who had a dermoid tumor was also categorized into the abnormal group. Thus the three groups are: normal (#1, #2, #5, #10 left ovary), abnormal (#3, #4, #6, #9, #10 right ovary) and malignant (#7, #8). The patients' information, injection dose, time delay between injection and measurement, the average total positron counts per 3 minutes and the count rates (average total counts/injection activity) as well as the standard deviations for these three categories are given in Table 1. The average count rate and standard deviation from normal, abnormal and malignant groups were 1.23 counts/MBq (0.38, $n = 7$), 1.44 counts/MBq (0.18, $n = 8$), and 10.78 (13.76, $n = 3$), respectively. On average, 1.2-fold higher total count rate was found between abnormal and normal groups, and 7.5- and 8.8-fold higher total count rates were found between malignant and abnormal, and malignant and normal groups, respectively. The range of count rates of the

Table 1. Patient characteristics and positron measurement (three minutes)

Category	Patient#	Age	Weight (kg)	Injection		Counts (std ^b , left)	Count rate (std ^b , left)	Counts (std ^b , right)	Count rate (std ^b , right)
				Activity (MBq)	TD ^a (min)				
Normal	#1	63	56	643.8	115	588(134)	0.91(0.21)	467(29)	0.72(0.04)
	#2	52	58	484.7	92	721(39)	1.49(0.08)	759(125)	1.57(0.26)
	#5	58	103	599.4	86	629(70)	1.05(0.12)	676(36)	1.13(0.06)
	#10 left	59	76	495.8	101	864(104)	1.74(0.21)		
Abnormal	#3	52	57	562.4	120	703(153)	1.25(0.27)	775(53)	1.38(0.09)
	#4	40	68	569.8	108	901(150)	1.58(0.26)	n/a	n/a
	#6	32	83	584.6	145	880(75)	1.51(0.13)	883(102)	1.51(0.17)
	#9	79	90	636.4	77	751(153)	1.18(0.24)	1098(140)	1.73(0.22)
	#10 right	59	76	495.8	101			684(140)	1.38(0.28)
Malignant	#7	68	78	514.3	85	1838(682)	3.57(1.33)	1095(244)	2.13(0.48)
	#8	61	70	543.9	91	n/a	n/a	14495(2127)	26.65(3.91)

^aTime difference between injection and measurement; ^bstd: standard deviation; ^cUnit: counts/MBq per 3 minutes.

normal and abnormal ovaries was 0.72 to 1.74 counts/MBq, and the range was 2.13 to 26.65 for malignant ovaries. In general, the count rates from left and right ovaries of the same patient were similar except patients #7, #9 and #10. For patient #7, we obtained lower count rate from the right ovary which had multiple surface tumor nodules compared with the left ovary which had extensive surface tumor nodules and masses invading into the ovarian cortex. For patient #10, the left ovary had adhesions due to lengthened resection process during surgery, resulting in an early acute inflammatory response with active hyperemia and margination of neutrophils. This may have caused the higher count rate compared with that of the right due to the increased local blood flow. For patient #9, the right side has higher count rate than that of the left which corresponds to an area of dense calcification in dense fibrous stroma. It is not clear whether this finding can be attributed to the fibrosis or the calcification. No associated necrosis or inflammation was seen in the histologic sections. The histopathology and OCT features of 18 ovaries from three groups are given in Table 2. In general, the normal ovarian stroma appears homogeneous, relatively hyperintense in OCT images. Cysts and follicles appear as signal void circumferential regions of variable size with well-defined boundaries. Corpus albicans, focal lymphocytes and calcifications appear as signal void or poor regions with variable size and shape. Carcinomas appear as either surface bumps with significant light shadowing or hyperintense bands embedded in poor images. One benign calcified, ossified dermoid tumor appears heterogeneous in OCT images. Because of the small sample size reported in this pilot study, the sensitivity and specificity of these features in predicting normal and malignant ovarian tissues are not available.

Table 2. Corresponding histopathology and OCT features of 18 ovaries obtained from 10 patients

Category	Histopathology	OCT
Normal (1, 2, 5, 10(left))	Homogeneous cortical stroma	Homogenous, hyperintense
	Corpus albicans near surface	Signal void region with variable shape and size
	Inclusion cysts	Signal poor region with circumferential shape
Abnormal (3, 4, 6, 9, 10(right))	Large simple cysts, large follicles	Well defined boundary
	Small simple cyst	Signal void region with circumferential shape
	Cellular ovarian cortical stroma	Well-defined two hyperintense layers
	Prominent calcification	Signal void region with variable shapes
	Focal lymphocytes	Signal void region with variable shapes
	Vasculatures, congested vessels	Signal poor bands, circles or variable shapes
Malignant (7, 8)	Calcified, ossified dermoid tumor	Heterogeneity, signal poor regions with variable shape and size
	Surface tumor nodules (serous carcinoma)	Circumferential or semi-circumferential bumps deposited on the surface
	Small amount of collagenous stroma	Hyperintense region with irregular pattern
	Corpora albicans	Signal void region with undefined bottom
	All carcinoma with bands of collagen	Hyperintense bands embedded in poor image

An example of a normal ovary obtained from the left side of a 58-year-old postmenopausal woman # 5 is shown in Fig. 2. It shows the positron distribution map (a), one representative B-scan OCT image selected from a sequence of co-registered OCT images (b), and the corresponding 40 \times H&E histology slide (c). As described in Section 2.3, photons received from each scintillating fiber were scattered over the $2.5 \times 2.5 \text{ mm}^2$ PSPMT detection surface and the outputs of the Anger logic were distributed within the circle that corresponded to each scintillating fiber as shown in Fig. 2(a). The positron count rate was 0.95 counts/MBq for this location. The homogeneous OCT image had some bright spots near the surface. The corresponding histology showed dense cortical stroma in the OCT imaging depth range.

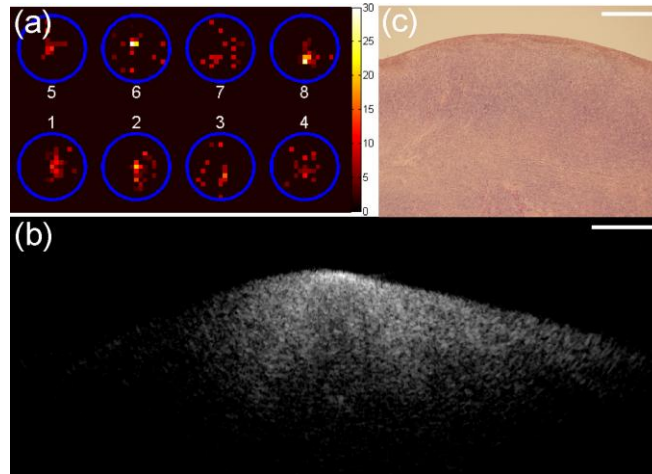


Fig. 2. One set of images obtained from the left ovary of normal patient #5. (a) Positron distribution map. (b) One representative OCT image obtained from a sequence of co-registered OCT images. (c) Corresponding 40 \times H&E histology. The OCT image size is 2 mm (depth) \times 5 mm (lateral) (height \times width); the histology size is 2 mm \times 2.6 mm (height \times width); the white scale bar is 0.5 mm.

An example of an abnormal ovary obtained from a 59-year-old postmenopausal woman #10 is shown in Fig. 3. The figure shows the positron distribution map (a), one representative B-scan OCT image selected from a sequence of co-registered OCT images (b), and the corresponding 40 \times H&E slide (c) obtained from the right ovary. The positron count rate was 1.47 counts/MBq in this area. The OCT image showed heterogeneous hyperintense bands corresponding to collagen bundles as marked by pink arrows and hypointense areas corresponding to blood vessels as marked by red oval arrows. These collagen bundles and blood vessels surrounded a dermoid tumor as marked by the yellow diamond arrow and were deeper than OCT could detect.

One set of images obtained from the left ovary of the abnormal patient #9 is shown in Fig. 4. The yellow ellipse in (a) is the map of the entire left ovary and the three solid squares represent three probe positions with the positron count rates shown inside the squares. 1.8-fold higher count rate was measured in the middle which indicated an abnormal local uptake of ^{18}F -FDG. Figure 4 (b) is the positron distribution map obtained at this location and an OCT image (c) revealed a well-defined void area. The corresponding 40 \times H&E shown in (d) revealed lymphocytes known to have higher metabolic activities than normal tissue and yielded a false positive in positron detection. However, the well-defined hypointense void area in OCT can help rule out malignancy. This example highlights the synergistic role of the hybrid probe in screening for both abnormal metabolic activity of early cancers and simultaneous high-resolution imaging of morphological details of the abnormality or early cancer.

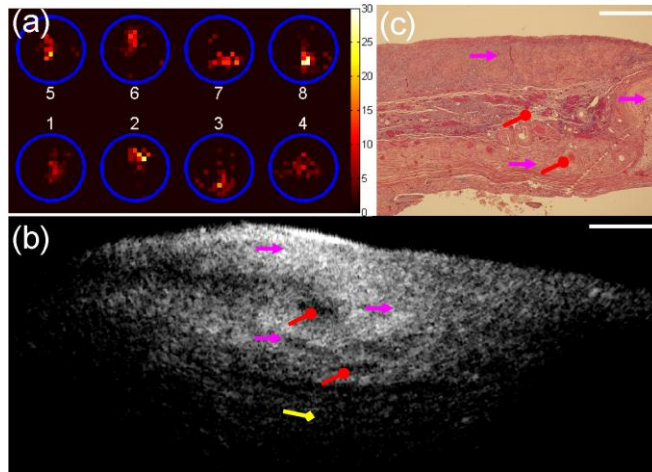


Fig. 3. One set of images obtained from the right ovary (abnormal) of patient #10. (a) Positron distribution map. (b) One representative OCT image obtained from a sequence of co-registered OCT images. (c) Corresponding 40× H&E histology. Pink arrow, collagen; red oval arrow, congested vessels; yellow diamond arrow, dermoid tumor. The OCT image size is 2 mm (depth) × 5 mm (lateral) (height × width); the histology size is 2mm × 2.6 mm (height × width); the white scale bar is 0.5 mm.

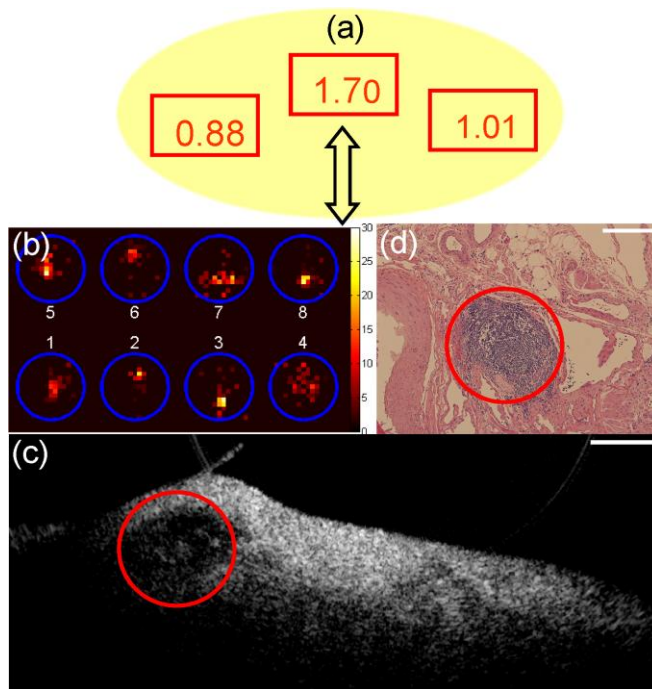


Fig. 4. One set of images obtained from the left ovary of abnormal patient #9. (a) Positron count rates from different locations of left ovary. (b) Positron distribution map from the location with highest count rate. (c) One representative OCT image obtained from a sequence of co-registered OCT images. (d) Corresponding 40× H&E histology. Red circle, lymphocytes. The OCT image size is 2 mm (depth) × 5 mm (lateral) (height × width); the histology size is 2mm × 2.6 mm (height × width); the white scale bar is 0.5 mm.

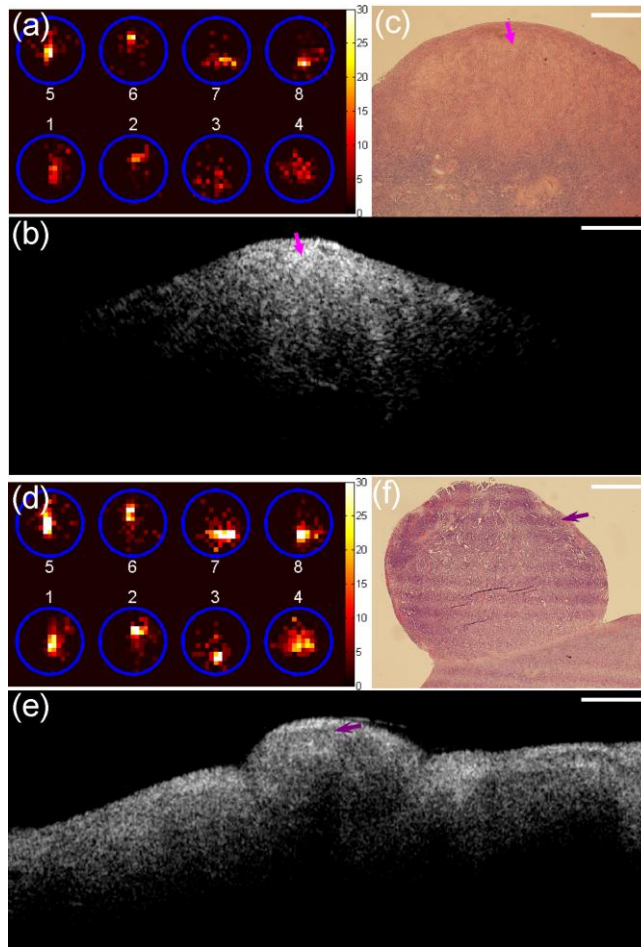


Fig. 5. Two sets of images obtained from the left ovary of patient #7 with malignant ovarian cancers. (a), (b) and (c) are from one side of the left ovary; (d), (e) and (f) are from the other side of the left ovary. (a) and (d): Positron distribution maps. (b) and (e) Representative OCT images obtained from a sequence of co-registered OCT images. (c) and (f) Corresponding 40 \times H&E histology. Pink arrow, collagen; purple stealth arrow, tumor nodule. The OCT image size is 2 mm (depth) \times 5 mm (lateral) (height \times width); the histology size is 2mm \times 2.6 mm (height \times width); the white scale bar is 0.5 mm.

An example of ovarian carcinoma obtained from a 68-year-old postmenopausal woman (patient #7) is shown in Fig. 5. Two sets of images were given with the first set (a-c) obtained from one side of the ovary and second set (d-f) from the opposite side of the ovary. The positron count rate (a) from the first set of data was 1.95 counts/MBq and 1.6 times higher than that obtained from normal ovaries. OCT image (b) showed high content collagen with irregular patterns which matched the collagen bundles marked in corresponding H&E slide (c). The positron count rate (d) obtained from the opposite side of the ovary was 5.04 counts/MBq and was 4.1 times higher than normal ovaries. The representative OCT image (e) clearly provided the nodule shape with significant light shadowing beneath the tumor nodule. The light shadowing was caused by the light absorption of the tumor. The corresponding H&E (f) showed the tumor nodule deposited on the ovary surface. Figure 6 shows one set of data obtained from the right ovary of the same patient #7. The positron count rate (a) from this location was 2.90 counts/MBq and was 2.4 times higher than that of the normal ovaries. The signal void region (red circle) shown in OCT image (b) corresponds to corpus albicans shown in the H&E histology (c) and the purple stealth arrows mark the cancer cells deposited on the

surface. It is interesting to note that the positron count rates were exquisitely sensitive to the amount of local tumor mass and could be potentially used as the screening tool during minimally invasive surgery for guiding the OCT to look into morphological changes in great details.

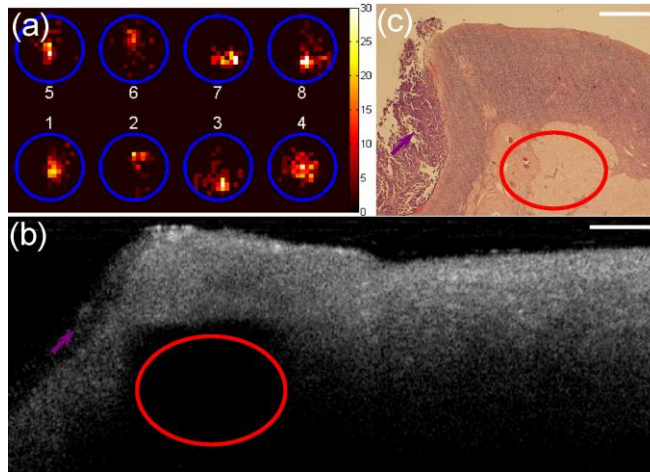


Fig. 6. One set of images obtained from the right ovary of patient #7 with ovarian cancers. (a) Positron distribution map. (b) One representative OCT image obtained from a sequence of co-registered OCT images. (c) Corresponding 40 \times H&E histology. Red circle, corpus albicans; purple stealth arrow, tumor. The OCT image size is 2 mm (depth) \times 5 mm (lateral) (height \times width); the histology size is 2mm \times 2.6 mm (height \times width); the white scale bar is 0.5 mm.

An example of advanced ovarian carcinoma obtained from a 61-year old postmenopausal woman is given in Fig. 7. This patient had ovarian cancer on both sides; however, only the right ovary was studied. The left ovary was not optimal for positron detection due to prolonged surgical time required for removal. The positron count rates (a) and (d) from the right ovary were 17~28 times higher than normal ovaries. OCT images revealed irregular patterns of hyperintense layers (b) and hyperintense regions (e) as marked in representative OCT images which represent a change in shape and directionality of the collagen fibers which were seen in the early cancers but are much more dramatic here. The H&E showed thick collagen bands embedded in the tumor cells (c) and (f) which matched the OCT hyperintense layers (b) and regions (e). This example demonstrates the great clinical potential of the dual-modality device for extremely sensitive detection of ovarian cancers.

4. Discussion

This study, to the best of our knowledge, reports the first *ex vivo* findings of positron count rates between malignant and abnormal/normal ovaries using ^{18}F -FDG as a tracer. The ratio of 7.5/8.8-fold higher was found between malignant and abnormal/normal ovaries. Other studies of thyroid cancer [6], head and neck cancer [31], colon and skin cancers [6], and metastatic melanoma [32], obtained from small patient pool of 5-26 using beta probes have reported various cancer to normal tissue ratios of 1.2-17.2.

In this study, the positron counting period was 3 minutes which could be long for surgeons to operate the device during laparoscopic surgical procedure. It is important to decrease the time needed for a quick diagnosis. Positron detectors with improved optical coupling between the scintillating fibers and the optical fibers and a detection circuitry with improved SNR have been developed during this one year clinical study period, which will improve the potential of this technology. The optimized detection circuitry and positron detector with better optical coupling and coating at the scintillator tip can effectively reduce the data acquisition time to 30 seconds without affecting detection sensitivity. However, in order to keep consistency with

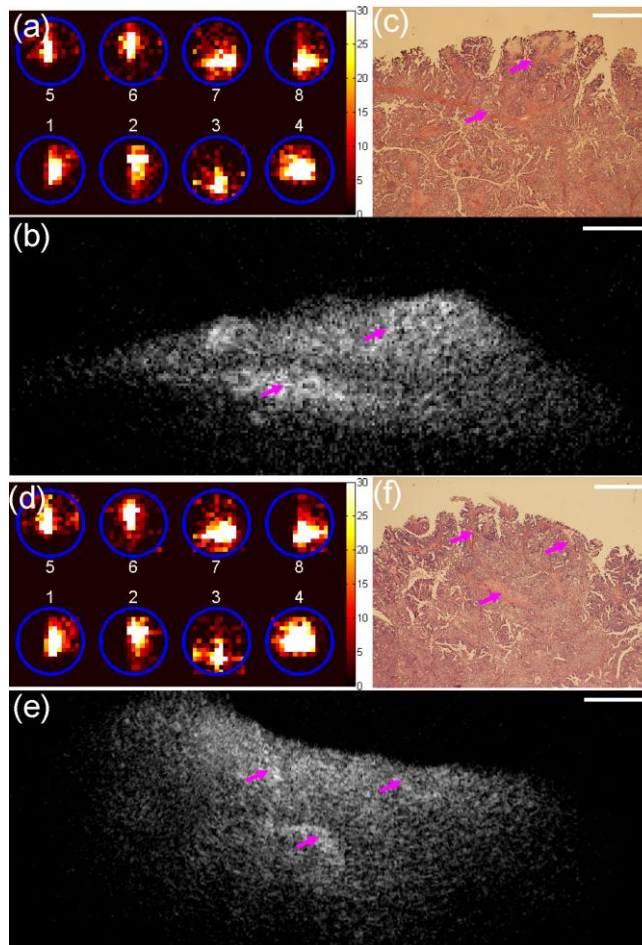


Fig. 7. Two sets of images obtained from the right ovary of patient #8 with ovarian cancers. (a), (b) and (c) are from one location; (d), (e) and (f) are from another location. (a) and (d) Positron distribution maps. (b) and (e) Representative OCT images obtained from a sequence of co-registered OCT images. (c) and (f) Corresponding 40 \times H&E histology. Pink arrow, collagen bundle. The OCT image size is 2 mm (depth) \times 5 mm (lateral) (height \times width); the histology size is 2mm \times 2.6 mm (height \times width); the white scale bar is 0.5 mm.

the data acquisition for all patients of different pathologies, we have used the reported system for all patients. In addition, a reduced rotational rate of 1 frame per 16 seconds was utilized in OCT system for the reported *ex vivo* studies. 10 frames per second which is adequate for *in vivo* study can be readily achieved by removing divider circuitry, improving data acquisition system and optimizing image processing code. Beyond this data acquisition speed, the rotation mechanics which could generate noise and OCT probe wobbling will need to be considered and an improved design will need to be implemented.

Our OCT imaging quality of ovarian tissue was comparable to that obtained by other research groups [24–27]. However, because of the large rotational scanning angle of the miniature ball lens catheter, the OCT imaging quality was poorer in general than the linear scanning images. Efforts are currently underway to optimize the OCT probe design and upgrade the OCT system to enable faster data acquisition and processing which will allow a larger number of averaging to improve OCT imaging quality.

In this study we have used the total counts from all positron detectors on the hybrid probe as a measure to quantify the ^{18}F -FDG uptake of each ovary. In principle, the weighted centroid algorithm on positron counts measured from all individual detectors can be used to

identify a small localized lesion with a high ^{18}F -FDG uptake [28]. However, because of the different coupling efficiency between the scintillators and optical fibers, the sensitivity variation among the reported positron detectors was more than 3:1 and this impeded the application of centroid algorithm. With the help of micro-fabrication techniques we could make repeatable and precise positron probes having uniform sensitivity. The gain variation of PSPMT channels can be compensated by calibration. In future studies we will apply the centroid algorithm using the improved detectors to help identify a small localized lesion with a high ^{18}F -FDG uptake.

In our *ex vivo* study, the ambient gamma background collected by the two beta-shielded detectors was in the noise level. However, this gamma background level could be much higher in *in vivo* imaging condition where the surrounding tissue would have significant ^{18}F -FDG uptake and produce gamma photons. We anticipate that the gamma subtraction will be needed in future *in vivo* study and the effectiveness of the subtraction will be tested.

Two major system design modifications are needed for fitting the intraoperative hybrid probe to a standard laparoscope accessory port of 5-12.5 mm diameter for *in vivo* evaluation of the ovary. The longitudinal distance of the current hybrid probe used in the reported study was more than 15 mm and the total width was more than 5mm. This relatively large size of the probe is the result of the optical fibers exiting the probe in the orthogonal arrangement as shown in Fig. 1(f), which makes it difficult to fit the entire probe within a 5-12.5 mm laparoscope accessory port. We are currently working on new designs that will allow the probe fit into a 5-12.5 mm laparoscope port for future *in vivo* evaluation during minimally invasive surgery.

Summary

In this report, the potential role of a prototype intraoperative probe combining positron detection and OCT imaging for ovarian cancer detection and characterization was evaluated using 18 *ex vivo* ovaries of various pathologic conditions. Positron count rates of 7.5/8.8-fold higher were found between malignant ovaries and abnormal/normal ovaries. OCT imaging of malignant and abnormal ovaries revealed many detailed morphologic features that could be potentially valuable for evaluating local regions with high metabolic activities and detecting early malignant changes of the ovary.

Acknowledgments

This research was supported by the Connecticut Department of Public Health under contract DPH# 2008-0121